ROYAL SOCIETY OF CHEMISTRY

PAPER

An efficient photocatalysis-self-Fenton system based on Fe(II)-MOF/g-C₃N₄ for direct hydroxylation of benzene to phenol†

Xu Jia,*[a] Xuetong Xu,[a] Cong Liu,[a] Fuying Wang,[a] Liuxue Zhang, [ID] *[a] Shuyan Jiao,*[a] Genxing Zhu,[a] Guomin Yu[a] and Xiulian Wang[b]

In order to avoid the issues causing weaknesses in the cumene method, a heterojunction catalyst based on Fe(II)-MOF/g-C₃N₄ was synthesized *via in situ* synthesis. The combination of Fe(II)-MOF and g-C₃N₄ was stable. With the synergistic effect of photocatalysis and the Fenton effect, the catalyst could achieve efficient direct hydroxylation of benzene to phenol. The yield and selectivity were 16.4% and 98.8% under the optimum conditions, respectively. And the catalytic activity of the heterojunction still sustained well after 5 reaction cycles. Hence, the explored photocatalysis-self-Fenton system could be applied in the field of direct hydroxylation of benzene to phenol.

Introduction

Phenol, an important industrial chemical, was widely used in the production of various chemical products and intermediates such as phenol resin and bisphenol A. Recently, the cumene method has been found to be the main way of industrial phenol production.[1] However, this method has some weaknesses such as high energy consumption, requirement of strong acids and low yield of phenol every time.[2] Due to the mild reaction conditions, small energy consumption, and few by-products, the direct hydroxylation of benzene to produce phenol has attracted wide attention. Nevertheless, most of the traditional benzene hydroxylation catalysts needed high temperature and high pressure, and the reaction of phenol was vigorous and it was easily overoxidized.[3] Photocatalysis is a green technology that converts renewable solar energy directly into chemical energy, and it could achieve direct hydroxylation of high-efficiency benzene to produce phenol.[4]

As a new type of porous crystal material, metal–organic frameworks (MOFs) have been widely applied in the field of photocatalysis with their large specific surface area, regular aperture, open pore channels and abundant catalytic sites.[5] In particular, due to the presence of extensive ferric oxygen (Fe–O)

clusters, iron-based MOFs were attractive in photocatalysis.[6] For instance, Zhang *et al.* prepared a mixed valent Fe-based MOF, which had an excellent catalytic performance in photo-catalytic hydrogen production.[7] In addition, due to the Fenton reaction, the iron-based MOFs could react with H₂O₂ to produce a hydroxyl radical, and the photocatalytic benzene hydroxylation could be achieved to prepare phenol.[8] Tu has synthesized a novel Fe-based MOF with a topological framework as a recyclable heterogeneous catalyst for benzene hydroxylation.[9] The Yang group reported a mixed valent Fe-based MOF, which greatly enhanced Fenton performance and further improved the efficiency of benzene hydroxylation to produce phenol.[10]

To a certain extent, although MOF materials could be applied to the direct hydroxylation of benzene to prepare phenol, its limited response to light impeded its wide application. Due to its graphene-like two-dimensional (2D) structure, suitable band gap (2.7 eV), visible light absorption, chemical and thermal stability, non-metallic properties and photocatalytic properties, C₃N₄ had attracted extensive attention as a sustainable material.[11] Sanny *et al.* had designed a bimetallic CuAg@g-C₃N₄ catalyst system by impregnating copper and silver nanoparticles on the surface of g-C₃N₄. It achieved ideal results in benzene hydroxylation under visible light.[12] In addition, when g-C₃N₄ was combined with an MOF, it facilitated not only the response of the MOF substrate to light, but also the diffusion of the reactants and products.[13] For instance, Fu *et al.* pointed out that the combination of g-C₃N₄ and MOF heterojunctions could greatly improve the efficiency of carrier separation and then photocatalytic activity.[14] Qi showed that the combination of g-C₃N₄ and MOFs not only facilitated the absorption of visible light, but also facilitated the separation of electrons and holes, thus improving the performance of the catalyst.[15]

[a] School of Materials and Chemical Engineering, Zhongyuan University of Technology, Zhengzhou, 450007, P. R. China. E-mail: jiax@zut.edu.cn, zhanglx@zut.edu.cn, jiaosy@zut.edu.cn; Fax: +86-731-62506095; Tel: +86-731-62506699

[b] School of Energy and Environment, Zhongyuan University of Technology, Zhengzhou, 450007, P. R. China

† Electronic supplementary information (ESI) available. See DOI: https://doi.org/10.1039/d3ma00235g

Herein, a novel photocatalyst Fe(ɪɪ)-MOF/g-C$_3$N$_4$ was prepared by an *in situ* composite technique. Fe-based MOFs can undergo the Fenton reaction with hydrogen peroxide to release hydroxyl radicals. g-C$_3$N$_4$ possesses a suitable band gap and could realize the efficient absorption of visible light. The combination of the Fe(ɪɪ)-MOF and g-C$_3$N$_4$ would exhibit synergistic effects of the Fenton effect and photocatalysis with relatively high yield and better selectivity in the direct hydroxylation of benzene to phenol. Therefore, the synthesized catalyst was expected to play an important role in the field of direct hydroxylation of phenol.

Experimental

Materials and synthesis

Ferrous acetate (>90%) was obtained from Shanghai Aladdin Biochemical Technology Co., Ltd. 1,4-Benzoquinone (97%) was obtained from Guangdong Wong Jiang Chemical Reagent Co., Ltd. 2-Aminoterephthalic acid (AR) was purchased from Zhengzhou Alfa Chemical Co., Ltd. 30% hydrogen peroxide and *N,N*-dimethylformamide (AR) were obtained from Tianjin Kemiou Chemical Reagent Co., Ltd. The other chemicals were commercially obtained and used without further purification.

Synthesis of the ferrous acetate MOF (Fe(ɪɪ)-MOF)

In order to embed unstable Fe^{2+} into the skeleton structure of MOF, Fe(ɪɪ)-MOF was prepared by the slight adjustment of the synthesis method reported by the Xu team.[16] Firstly, Ferrous acetate (1.2 g, 6.90 mmol) was dissolved in 15 mL DMF/ethanol mixture (V/V, 1:1). And then, 30 mL DMF solution containing 2-aminoterephthalic acid (1.0 g, 5.52 mmol) was slowly injected into the abovementioned solution under stirring at room temperature. When the solution was mixed evenly, the reaction was heated to 45 °C and stirring was continued for 1 h at a speed of 500 rpm under nitrogen. The product was collected by centrifugation and washed with ethanol several times, dried in a vacuum, and labeled as Fe(ɪɪ)-MOF for further use.

Synthesis of layered g-C$_3$N$_4$ nanosheets

Layered g-C$_3$N$_4$ nanosheets were prepared by a two-step calcination method. A certain amount of melamine was transferred into a quartz boat and placed in a closed tubular furnace. The temperature was increased to 550 °C at a heating rate of 5 °C min^{-1}, kept for 2 hours, and then the reaction was continued in a flowing air atmosphere for 4 hours. After cooling to room temperature, the grinder ground light yellow powder was labeled g-C$_3$N$_4$.[17]

Synthesis of Fe(ɪɪ)-MOF/g-C$_3$N$_4$ composites

The synthesis procedure for Fe(ɪɪ)-MOF/g-C$_3$N$_4$ was similar to that described above for the preparation of Fe(ɪɪ)-MOF, except that 0.5 g of layered g-C$_3$N$_4$ powder was added to the solution before the addition of 2-aminoterephthalic acid. Then the reaction time was extended to 4 h. The prepared sample was labeled as Fe(ɪɪ)-MOF/g-C$_3$N$_4$.[16]

Characteristics conditions of photocatalytic hydroxylation

The evaluation of photocatalytic performance was carried out in quartz reactors. The LED lamp (5 W) which emitted simulated sunlight full spectrum irradiation (380–760 nm) was used as the light source. Specifically, Fe(ɪɪ)-MOF/g-C$_3$N$_4$ composites, acetonitrile, trifluoroacetic acid and benzene were added to the reactor, and gently stirred for a period of time. When the temperature of the solution was increased to the setting temperature, the lamp was turned on. H$_2$O$_2$ was titrated into the solution within 30 min. The reaction was maintained for a period. Then, the solution was treated by centrifugation. The qualitative and quantitative analysis of the supernatant was performed using toluene as an internal standard by gas chromatography–mass spectrometry (GC–MS qp2010) and gas chromatography (Agilent 6820). In parallel research experiments, the best reaction conditions were explored by adjusting the ratio of H$_2$O$_2$ and benzene, reaction time and solvent.

The conversion of benzene, the selectivity of phenol and the yield of phenol are calculated as follows:

$$C \text{ (conversion of benzene)} = 1 - \frac{\text{the mol of the residual benzene}}{\text{the mol of the initial benzene}} \times 100\%$$

$$S \text{ (selectivity of phenol)} = \frac{\text{the mol of generated phenol}}{\text{the mol of invert benzene}} \times 100\%$$

$$Y \text{ (yield of phenol)} = \frac{\text{the mol of generated phenol}}{\text{the mol of the initial benzene}} \times 100\%$$

Characterization of the Fe(ɪɪ)-MOF/g-C$_3$N$_4$ composites

The morphology of the catalysts was verified by scanning electron microscopy (Phenom Prox) with an operating voltage of 10 kV. The X-ray diffraction (Rigaku Ulitima IV) pattern was obtained with Cu Kα radiation at a scan speed of 10 min^{-1} from 5 to 60°. The steady-state photoluminescence was tested on a Hitachi F-7100 spectrofluorometer at room temperature. The transient photocurrent measurements, electrochemistry impedance spectroscopy (EIS) and Mott–Schottky plots were evaluated using the electrochemical workstation (CHI600E). The electrochemical information was collected using a standard three-electrode cell: Ag/AgCl electrode (SCE) as the reference electrode and Pt electrode as the counter electrode. The working electrode was prepared using a rectangular FTO glass sheet (2 cm × 1 cm) on which was spread 50 μL *N,N*-dimethylformamide solution of photocatalysts (10 mg mL^{-1}) evenly. The prepared electrode should be dried in the oven at 80 °C for 2 h.

The quantitative analysis of phenol was performed by gas chromatography (Techcomp GC7900), the injection port temperature was 210 °C, FID was selected as the detector and the temperature was set at 240 °C.

Results and discussion

Sample structure characterization

The crystal structure of the photocatalyst was characterized and analyzed using an X-ray diffractometer. As shown in Fig. 1(a),
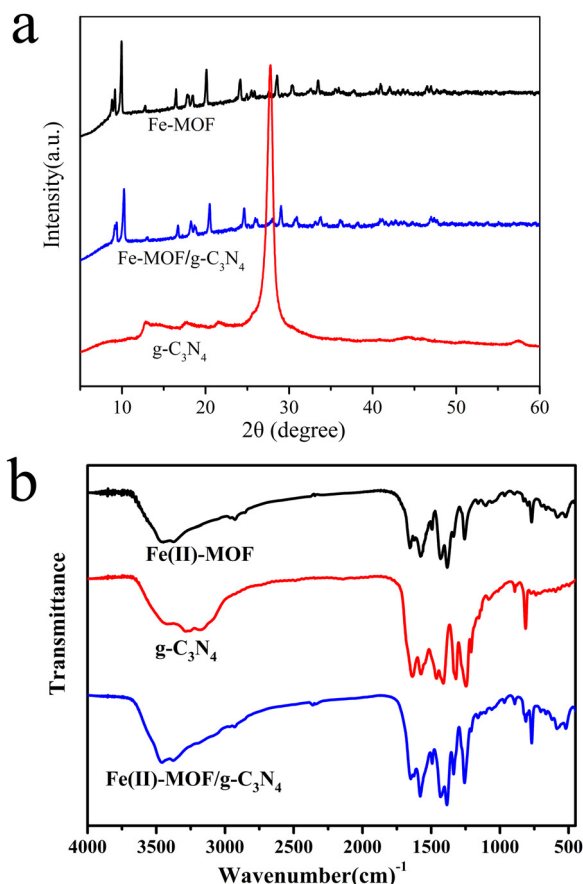
Fig. 1 XRD patterns (a) and infrared spectra (b) of Fe(II)-MOF, layered g-C$_3$N$_4$, and Fe(II)-MOF/g-C$_3$N$_4$.

a series of diffraction peaks of Fe(II)-MOF could be observed such as $9°$, $11.8°$, $18.08°$, $18.99°$, $22.25°$, $27.6°$, and $30.9°$, which were consistent with the results reported in the related literature, and no other impurity peaks were observed, that indicated the Fe(II)-MOF material was successfully prepared in the experiment, and the synthesized material had high crystallinity.[18] In addition, it could be clearly observed that the Fe(II)-MOF/g-C$_3$N$_4$ and Fe(II)-MOF had very similar XRD peaks, which confirmed that the incorporation of g-C$_3$N$_4$ did not change the stable skeleton structure of MOF material, and a new smaller peak was found at $2\theta = 27.7°$ in the XRD diffraction pattern of the composite material, which could be considered a typical interlayer stack peak (002) attributed to g-C$_3$N$_4$.[19] Therefore, XRD results indicated that the two materials were successfully combined.

Fourier infrared spectroscopy was used as an analytical tool to characterize the structural characteristics of photocatalyst samples. As shown in Fig. 1(b), the absorption peaks near 1643 cm^{-1} and 1427 cm^{-1} were attributed to the symmetric and asymmetric stretching of –COOH in the backbone of the organic ligand (2-amino terephthalate) connected to Fe^{2+}, respectively, which proved that it contained the carboxyl group.[16] In addition, the absorption peak at 521 cm^{-1} corresponded to the vibration peak of Fe–O, which further confirmed the formation of the Fe(II)-MOF material.[20] For layered g-C$_3$N$_4$, the wide absorption

band between 3000 cm^{-1} and 3500 cm^{-1} was caused by the N–H and O–H stretching patterns. The sharp absorption band at 812 cm^{-1} was attributed to the bending vibration absorption of the carbon nitrogen ring (C–NH–C) in the triazine ring structure.[21] Peaks at 1633 cm^{-1} and 1247 cm^{-1} were associated with the typical –C=N– tensile vibrations of heptazine derived repeat units and the C–N stretching of aromatic groups, respectively.[22] When g-C$_3$N$_4$ was introduced into MOF, the same position peak as mentioned above could be observed in the spectrum of the composite material, that confirmed the successful preparation of Fe(II)-MOF/g-C$_3$N$_4$. It was worth noting that the peak intensity of g-C$_3$N$_4$ was generally reduced, which might be caused by the low content in the composite material, which was consistent with XRD results.

The surface morphology and elemental distribution information of samples were obtained by scanning electron microscopy and EDS analysis. The Fe(II)-MOF exhibited a small and uniform spindle-like morphology (Fig. 2(a) and Fig. SI1, ESI†).[24] As shown in Fig. 2(b), layered g-C$_3$N$_4$ formed by continuous calcination of melamine in tubular furnace obviously presented a stacked sheet structure and had a larger specific surface area than the massive g-C$_3$N$_4$, which was favorable for photocatalytic reactions.[23] And it could be observed that Fe(II)-MOF and g-C$_3$N$_4$ were tightly bound together (Fig. 2(c)), the relatively large particle size might be caused by the longer reaction time of the composite than that of pure Fe(II)-MOF. And then, the EDS results showed that Fe, C and N elements were uniformly distributed on the composite material, which could prove the successful preparation of Fe(II)-MOF/g-C$_3$N$_4$.

In order to better analyze the composition and valence of the elements on the surface of the photocatalyst sample, the X-ray photoelectron spectra of the prepared sample were tested, and the results are shown in Fig. 3(a). The full-scan spectrogram of Fe(II)-MOF/g-C$_3$N$_4$ further proved the presence of Fe, C, N and O in the composite sample, which was consistent with the EDS results. The high-resolution C 1S XPS spectrum could be decomposed into four peaks located at 284.8 eV (C1), 285.9 eV (C2), 287.0 eV, (C3) and 288.7 eV (C4) (Fig. 3(b)). Major C1 was usually attributed to standard carbon, while C2 and C4 peaks at 285.9 and 288.7 eV were attributed to carboxyl groups (O–C=O) in organic ligands.[25] The smaller peak (287.0 eV) C3 in the photocatalytic composite Fe(II)-MOF/g-C$_3$N$_4$ was assigned to sp^2 hybrid carbon atoms (N–C=N) in g-C$_3$N$_4$.[26] The N 1s XPS spectra
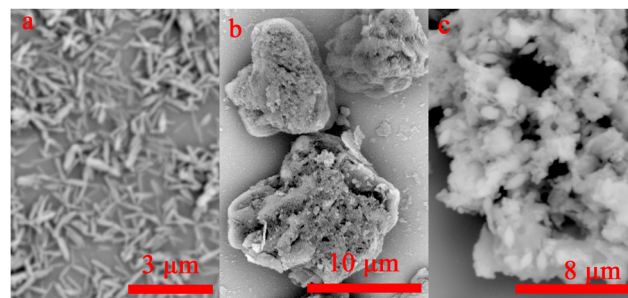

Fig. 2 SEM images of (a) Fe(II)-MOF, (b) layered g-C$_3$N$_4$, (c) Fe(II)-MOF/g-C$_3$N$_4$.
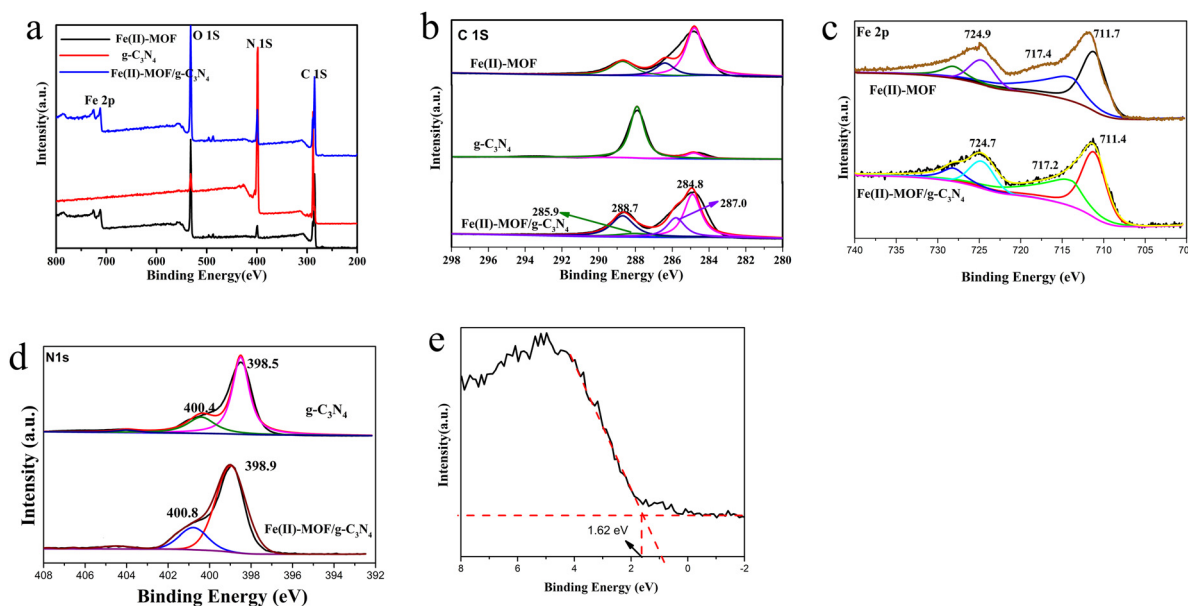
Fig. 3 Full spectrum comparison of XPS of (a) Fe(II)-MOF, layered g-C₃N₄, and Fe(II)-MOF/g-C₃N₄; high resolution XPS of (b)C 1S (c) Fe(II) 2p, (d) N 1s and ()valence band (VB) XPS spectra of Fe(II)-MOF/g-C₃N₄.

of the two samples were deconvoluted into three peaks located at 398.5 and 400.4, corresponding to bicoordinated nitrogen (N_{2C}), and tricoordinated nitrogen (N_{3C}) in the heptazine framework, respectively (Fig. 3(e)).[27] By analyzing the high-resolution XPS spectrum of Fe 2p of Fe(II)-MOF/g-C₃N₄ (Fig. 3(c)), three peaks could be further fitted, and peaks with binding energies of 711.4 eV, 717.3 eV and 724.7 eV could be assigned to Fe^{2+} 2p3/2, satellite peaks and Fe^{2+} 2p1/2, respectively.[28] The binding energy difference between the Fe 2p3/2 peak and the satellite peak is approximately 6 eV. The presence of this "shoulder" satellite peak and the binding energy difference of 6 eV are consistent with the results obtained by other researchers, and are clear evidence of the existence of Fe^{2+}.[29–31] The binding energy of the composite peak was slightly higher than that of Fe(II)-MOF, which proved the rapid transfer of electrons and the characteristic of the formation of a heterojunction.

Performance study of the photocatalytic benzene hydroxylation system

Effect of different catalysts on the hydroxylation of benzene to phenol. The benzene hydroxylation properties of the photocatalysts Fe(II)-MOF, g-C₃N₄ and Fe(II)-MOF/g-C₃N₄ in pure acetonitrile solvents were compared with hydrogen peroxide as the oxidant. The experimental results are illustrated in Table 1. A lower phenol yield could be detected in the post-reaction products catalyzed by g-C₃N₄, and the yield was only 4.6%. Compared with g-C₃N₄, the catalyst Fe(II)-MOF could achieve a benzene conversion rate of 6.5%. Under the same conditions, when the composite Fe(II)-MOF/g-C₃N₄ was used as a catalyst, it exhibited higher photocatalytic performance than any single component (16.6% phenol yield and 98.8% phenol selectivity). Therefore, the best performance of Fe(II)-MOF/g-C₃N₄ was selected as the photocatalyst for benzene hydroxylation to make phenol in the following experimental exploration.

Table 1 Effect of different photocatalysts on benzene hydroxylation to produce phenol

Entry	Yield (%)	Conversion (%)	Selectivity (%)
1	6.1	6.5	93.8
2	4.6	4.9	93.9
3	16.4	16.6	98.8
4	7.8	8.0	97.0

Reaction conditions: catalyst (1: Fe(II)-MOF, 2: g-C₃N₄, 3: Fe(II)-MOF/g-C₃N₄, Fe(II)-MOF + g-C₃N₄ mixture) (1–3: 20 mg, 4: Fe(II)-MOF 14 mg, g-C₃N₄ 6 mg), benzene (1.6 mL, 18.05 mmol), H_2O_2 (30 wt%) (0.6 mL), acetonitrile: 11 mL, trifluoroacetic acid: 0.1 g, trifluoroacetic acid: 0.1 g, time: 4 h and T: 333 K

Effect of the catalyst amount

In order to investigate the effect of the amount of Fe(II)-MOF/g-C₃N₄ on the performance of benzene hydroxylation to phenol, catalyst samples of different amounts were added under the conditions of 1.6 mL substrate benzene, 11 mL acetonitrile and 0.6 mL oxidant H_2O_2. The photocatalytic performance of the system was tested at 60 °C for 4 h. As illustrated in Table 2, when there was no photocatalyst, direct hydroxylation was difficult for benzene under light irradiation, and almost no phenol was generated. With the increase of photocatalyst amount, the performance of benzene hydroxylation reaction was greatly improved, mainly because more catalysts could satisfy the quantity of Fe^{2+} required for the Fenton reaction, and more ·OH was generated to react with the benzene ring to produce phenol.[32,33] When the catalyst amount was further increased, the yield of phenol decreased. Similar phenomena could be found in previous references. More catalyst powder in the photocatalytic process might cause the shielding effect, leading to the decrease of light utilization. Moreover, excessive production of hydroxyl radicals led to the self-quenching side reaction. The self-quenching reaction had a

Table 2 The effect of the amount of catalyst on the catalytic benzene hydroxylation

Entry	m (mg)	Yield (%)	Conversion (%)	Selectivity (%)
1	0	0.8	0.97	82.0
2	10	11.7	12.1	96.7
3	20	16.4	16.6	98.8
4	30	13.6	14.0	97.1
5	40	10.9	11.3	96.5

Reaction conditions: benzene (1.6 mL, 18.05 mmol), H_2O_2 (30 wt%) (0.6 mL), acetonitrile: 11 mL, trifluoroacetic acid: 0.1 g, t = 4 h and T = 333 K

Table 4 Effect of the amount of trifluoroacetic acid on the catalytic benzene hydroxylation

Entry	Mass of TFA (g)	Yield (%)	Conversion (%)	Selectivity (%)
1	0	7.0	7.3	95.9
2	0.05	10.5	10.8	97.2
3	0.10	16.4	16.6	98.8
4	0.15	13.0	13.3	97.7
5	0.20	9.2	9.5	96.8

Reaction conditions: catalyst (20 mg), benzene (1.6 mL, 18.05 mmol), H_2O_2 (30 wt%) (0.6 mL), acetonitrile: 11 mL, time: 4 h and T: 333 K.

fast reaction rate, which was not conducive to the hydroxylation of the benzene reaction. Therefore, the optimal catalyst quality was 20 mg from performance and economic considerations.[34–38]

Effect of the amount of hydrogen peroxide

In the reaction system of photocatalytic benzene hydroxylation, the amount of oxidant (hydrogen peroxide) was another key factor which affected the activity of benzene hydroxylation to phenol. 20 mg of the Fe(ɪɪ)-MOF/g-C$_3$N$_4$ catalyst, 1.6 mL of benzene and 0.1 g of co-catalyst trifluoroacetic acid were transferred to 11 mL of acetonitrile solvent with different volume ratios of benzene and hydrogen peroxide (8:1, 8:2, 8:3, 8:4 and 8:5). The effect of H_2O_2 addition to benzene hydroxylation to phenol was detected at 60 °C for 4 h. As illustrated in Table 3, the photocatalyst could harvest the optimal benzene hydroxylation to phenol, phenol yield and selectivity were 16.4% and 98.8%, respectively, under a volume ratio of 8:3. However, only a lower phenol yield was obtained at a higher volume ratio. This might be caused by the reasons that the higher H_2O_2 concentration to capture the hydroxyl radical was strong which reduced its amount in solution,[39] and excessive oxidants would not only further convert phenol into by-products, but also lack economic and environmental protection in practical applications. Therefore, the optimal amount of hydrogen peroxide was 0.6 mL for this experiment.

Effect of the trifluoroacetic acid amount

When acetonitrile was selected as the reaction solvent, studies had shown that the co-catalyst trifluoroacetic acid would help the system to form a uniform system between the composite and the reaction medium.[40] To further investigate the extent of influence of trifluoroacetic acid on the photocatalytic reaction, the masses of the cocatalyst were 0 g, 0.05 g, 0.10 g, 0.15 g and 0.20 g without changing the other reaction conditions, and the

results are illustrated in Table 4. When the cocatalyst was not used in the photocatalytic process, the conversion rate of benzene was only 7.3%. When the addition of trifluoroacetic acid was 0.1 g, the best benzene conversion rate (16.6%), phenol yield (16.4%) and selectivity (98.8%) could be obtained. When the amount of trifluoroacetic acid was further increased, the photocatalytic performance was reduced. Similar phenomena have been studied in the published references. The decrease of the hydroxylation of benzene at a higher amount of CF$_3$COOH was apparently due to the decomposition of substantial amount of H_2O_2 via the Fenton reaction to facilitate hydroxyl radical generation before attaining the maximum reaction rate. Indeed, the part of hydroxyl radicals which was involved in the hydroxylation of benzene was decreased, while the part of which led to the self-quenching side reaction was increased.[41–45] Therefore, the optimum amount of trifluoroacetic acid was 0.1 g in this system.

Effects of the reaction time and temperature

The effect of different reaction times on the selective catalytic oxidation of benzene by Fe(ɪɪ)-MOF/g-C$_3$N$_4$ is illustrated in Table 5. The experiment of hydroxylation reactions was taken at different times such as 1 h, 2 h, 3 h, 4 h and 5 h. The reaction time had an important impact on the yield of phenol, initially the yield increased with the increase of the reaction time, and then the yield decreased as the time continues to extend. When the reaction lasted for 4 h, the selectivity of phenol reached 98.9%, and the conversion of benzene also increased to 16.6%. And the yield of phenol decreased slightly with the extension of the reaction time, which might be caused by the oxidation of phenol.

The influence of the reaction temperature was also investigated on the photocatalytic reaction, the experimental systems were placed at 50, 60 and 70 °C respectively. As illustrated in Table 6, initially, the yield increased with the increase of temperature, and then the yield decreased as the temperature continued to

Table 3 The effect of the added amount of H_2O_2 on the catalytic benzene hydroxylation

Entry	$n(H_2O_2)/n(benzene)$	Yield (%)	Conversion (%)	Selectivity (%)
1	1/8	2.5	2.6	96.2
2	2/8	7.5	7.8	96.2
3	3/8	16.4	16.6	98.8
4	4/8	12.7	13.0	97.7
5	5/8	11.0	11.3	97.3

Reaction conditions: catalyst (20 mg), benzene (1.6 mL, 18.05 mmol), acetonitrile: 11 mL, trifluoroacetic acid: 0.1 g, time: 4 h and T: 333 K

Table 5 Effect of the reaction time on the catalytic benzene hydroxylation

Entry	t (h)	Yield (%)	Conversion (%)	Selectivity (%)
1	1	6.6	6.7	98.5
2	2	10.1	10.3	98.1
3	3	14.3	14.6	97.9
4	4	16.4	16.6	98.8
5	5	15.3	16.9	90.5

Reaction conditions: catalyst (20 mg), benzene (1.6 mL, 18.05 mmol), H_2O_2 (30 wt%) (0.6 mL), acetonitrile: 11 mL, trifluoroacetic acid (0.1 g) and T = 333 K

Table 6 Effect of the reaction temperature and light on the benzene hydroxylation reaction

T (°C)	Yield (%)	Conversion (%)	Selectivity (%)
50	11.8	12.2	96.7
60	16.4	16.6	98.8
70	14.3	14.8	96.6
60^d	11.1	13.7	81.1

Reaction conditions: catalyst (20 mg), benzene (1.6 mL, 18.05 mmol), H_2O_2 (30 wt%) (0.6 mL), acetonitrile: 11 mL, trifluoroacetic acid: 0.1 g and t = 4 h, 60^d: 60 °C in dark.

rise. The best benzene conversion and phenol selectivity was obtained at 60 °C. That might be because the higher reaction temperature was favorable for the generation of active radicals required during photocatalysis, which accelerated the photocatalytic reaction and increased the benzene conversion and yield of phenol to 16.6% and 16.4%, respectively. The photocatalytic performance of Fe(II)-MOF/g-C$_3$N$_4$ decreased when the reaction temperature reached 70 °C. The self-decomposition of hydrogen peroxide and the deep oxidation of phenol might be caused by the high temperature. And the reaction temperature increased close to the boiling point of benzene, it was easy to lead to the volatilization of the reactant.[46] Therefore, the optimal time for benzene hydroxylation was 4 h and the optimal temperature was 60 °C.
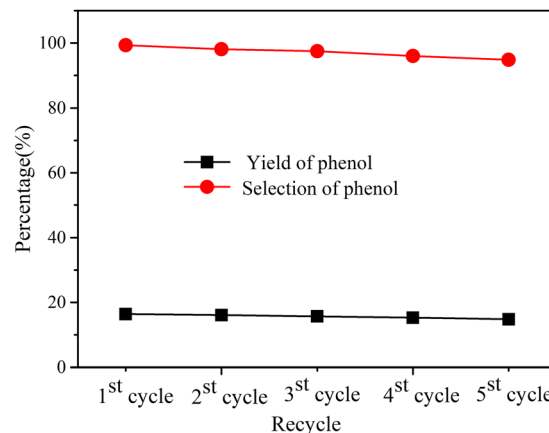
Performance study of the photocatalytic cycle

Considering the economic benefits and the full utilization of materials, it was essential to further study the regeneration and reusability of photocatalysts. Therefore, the recycling ability of Fe(II)-MOF/g-C$_3$N$_4$ as a heterogeneous photocatalyst was investigated. After the photocatalytic reaction, the catalyst was collected by centrifugation and washed with ethanol the regenerated catalyst was used under the optimal experimental conditions. As shown in Fig. 4, the photocatalytic performance of Fe(II)-MOF/g-C$_3$N$_4$ maintained well after five cycles, and the benzene conversion rate was 14.7%, which was close to the yield with the fresh catalyst. This result proved that the photocatalyst was highly stable and could be recycled.

A comparative study of Fe(II)-MOF/g-C$_3$N$_4$ MOFs and other photocatalysts previously reported for the photocatalytic hydroxylation of benzene to phenol was conducted, and the results are shown in Table 7. The phenol selectivity (99%) and yield (16.4%) obtained using the Fe(II)-MOF/g-C$_3$N$_4$ photocatalyst were higher than or comparable with those obtained using other photocatalysts.

Enhancement of photocatalytic performance and exploration of the process mechanism

Factors for improving photocatalytic performance. The light absorption characteristics of the sample could be understood by using the solid UV-visible diffuse reflection test, so as to further study the band structure of photocatalyst samples. As shown in Fig. 5, a single Fe(II)-MOF material had a wide light absorption range of absorbing light from the UV region to the visible region, where the wide absorption band displayed within a wavelength of 400 nm is concerned with the π–π* transition in the NH$_2$-BDC ligand and the band gap is 1.18 eV.[52] The light

Fig. 4 Recycling of Fe(II)-MOF/g-C$_3$N$_4$. Reaction conditions: catalyst (20 mg), benzene (1.6 mL, 18.05 mmol), H_2O_2 (30 wt%) (0.6 mL), acetonitrile: 11 mL, trifluoroacetic acid: 0.1 g, t = 4 h and T = 333 K.

Table 7 Comparison of photocatalytic activity of Fe(II)-MOF/g-C$_3$N$_4$ with other reported photocatalysts for the photocatalytic hydroxylation of benzene to phenol

Sample	Amount (mg mL^{-1})	Time (h)	Yield (%)	Ref.
FeVO$_4$@Al$_2$O$_3$	3.75	4	13.6	47
ZFO@C-2	5	—	15.5	48
FePc	6	4	15.2	49
UiO-66-NH$_2$-SA-V	1.5	4	15.3	50
Fe-g-C$_3$N$_4$/SBA-15	5.5	4	12.0	51
Fe(II)-MOF/g-C$_3$N$_4$	1.5	4	16.4	This work

absorption capacity of the material in the visible light region was attributed to the existence of the Fe–O cluster of the iron-metal–organic framework material itself.[53] A single g-C$_3$N$_4$ with absorption range from 200 nm to 450 nm had poor response to visible light and the band gap is 2.54 eV. Compared with Fe(II)-MOF, highly similar absorption spectra appeared in the composite Fe(II)-MOF/g-C$_3$N$_4$, and its optical absorption intensity increased significantly in the wavelength range of 200–620 nm and the band gap is 1.56 eV, which proved that the composite had better optical absorption capacity.

The high photogenic-hole charge separation effect played an important role in photocatalytic phenol production. Therefore, the photoluminescence behavior of Fe(II)-MOF, g-C$_3$N$_4$, and Fe(II)-MOF/g-C$_3$N$_4$ were determined at an emission wavelength of 375 nm. Due to the fluorescence quenching behavior of 2-aminoterephthalic acid and Fe^{2+}, the fluorescence intensity of the single Fe(II)-MOF material was close to the baseline (Fig. 6(a)). However, when the Fe(II)-MOF combined with the g-C$_3$N$_4$, Fe(II)-MOF/g-C$_3$N$_4$ showed a lower fluorescence intensity than the g-C$_3$N$_4$ at a wavelength of 440 nm. These results indicated that Fe(II)-MOF/g-C$_3$N$_4$ had a higher photogenerated hole–charge separation efficiency.

The electrochemical impedance was also employed to further observe the effect of introducing g-C$_3$N$_4$ on photogenic charge–hole on recombination. The EIS Nyquist curves of g-C$_3$N$_4$, Fe(II)-MOF and Fe(II)-MOF/g-C$_3$N$_4$ electrodes were recorded under light avoidance conditions (Fig. 6(b)). The smaller the radius of the Nyquist circle,
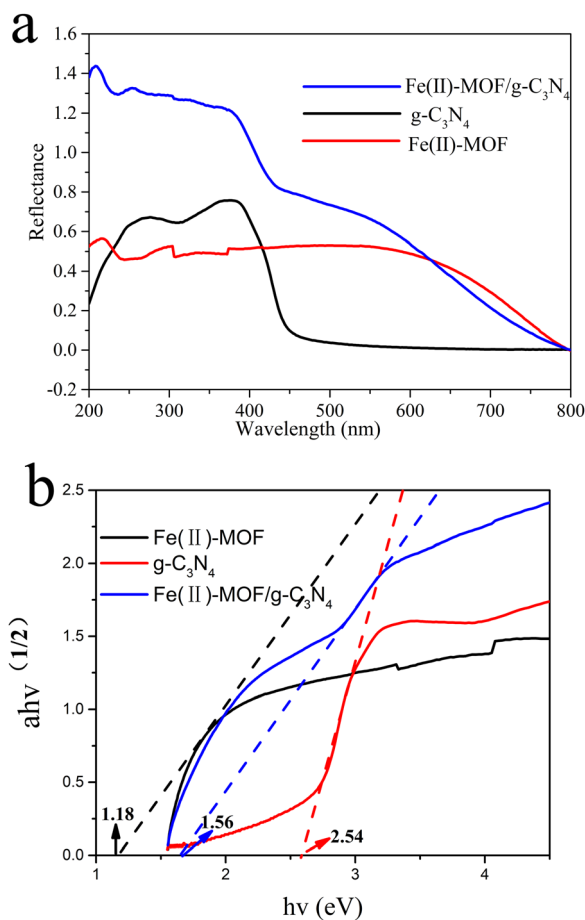
Fig. 5 Solid UV diffuse reflection of Fe (II)-MOF, layered g-C_3N_4, and Fe(II)-MOF/g-C_3N_4 (a) and band gap diagram of layered g-C_3N_4, and Fe(II)-MOF/g-C_3N_4 (b).

the smaller the transfer resistance, which indicated the lower the recombination rate of photogenerated carriers. Therefore, the separation efficiency of the electron–hole pair of Fe(II)-MOF/g-C_3N_4 was significantly higher than that of Fe(II)-MOF and g-C_3N_4.

In order to explore the influence of g-C_3N_4 introduction on the band structure, Mott–Schottky curves of g-C_3N_4, Fe(II)-MOF and Fe(II)-MOF/g-C_3N_4 catalysts were obtained by the Mott–Schottky measurement method (Fig. 6(c)). The curves reveal that the tangent line presents a positive slope at a frequency of 1000 Hz, which indicated that g-C_3N_4, Fe(II)-MOF and Fe(II)-MOF/g-C_3N_4 were all typical N-type semiconductors. The optical properties of Fe(II)-MOF/g-C_3N_4 were measured by using UV-vis absorption spectra (Fig. 5(a)), and the intrinsic optical bandgap energy (E_g) was calculated according to the Kubelka–Munk function (Fig. 5(b)). Then the E_g of Fe(II)-MOF/g-C_3N_4 was determined to be 1.56 eV by transforming the plots of absorption spectra. The measured flat band potential of Fe(II)-MOF/g-C_3N_4 was obtained to be −1.11 eV vs. RHE by fitting the Mott–Schottky plots in Fig. 6(c). As shown in Fig. 6(e), the valence band (VB) XPS spectra of Fe(II)-MOF/g-C_3N_4 were recorded and their VB was calculated to be 0.51 eV. Furthermore, the conduction band (CB) positions of samples were calculated to be −1.05 eV vs. RHE based on the $E_{CB} = E_{VB} - E_g$.[54,55]

In conclusion, as the composite rate of photo charged holes could be effectively suppressed, the photocarrier life could be extended, and the photoelectron could be effectively transferred to produce active free radicals, which could be applied for the photocatalytic benzene hydroxylation reaction.
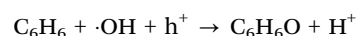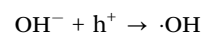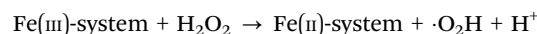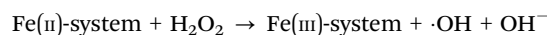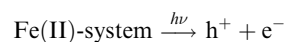
Generally, the photocatalytic activity was reflected by the photocurrent intensity, the better photocatalytic activity usually resulted by the higher photocurrent intensity.[56] Therefore, the separation efficiency of photoinduced charges in the photochemical reactions was characterized by the technique of the transient photocurrent measurement. As shown in Fig. 6(d), the composite Fe(II)-MOF/g-C_3N_4 possessed a distinctly higher photocurrent density than UiO-66-NH$_2$ under the same conditions. This result revealed that the recombination of photogenerated carriers was inhibited after it was compounded with g-C_3N_4.

Photocatalytic mechanism

Free radical capture detects the active substance. The main active substances involved in the photocatalytic benzene hydroxylation process are h$^+$, e$^-$, and ·OH.[57] In order to clarify the mechanism of the Fe(II)-MOF/g-C_3N_4 material in the process of benzene hydroxylation to produce phenol, the active substance that played a major role in the reaction were determined by free radical trapping experiments under the optimal conditions. Isopropanol (IPA), potassium dichromate and disodium ethylenediaminetetraacetate (EDTA-2Na) were employed as scavengers of hydroxyl radical (·OH), electron (e$^-$) and hole (h$^+$), respectively. As shown in Fig. 7, it was obvious that the addition of three capture agents all had an effect on the yield of phenol, and the addition of IPA greatly inhibited the photocatalytic process. This indicated that the phenol production process was mainly driven by the participation of hydroxyl radicals.

Basic reaction mechanism

According to the reported work and the experimental results, a possible photocatalytic mechanism of benzene hydroxylation to phenol was proposed in Fig. 8. In this process, visible light irradiation promotes the generation of the intermediate free radicals, contributing to the catalytic performance, and then, Fe(II)-MOF/g-C_3N_4 reacts with H_2O_2 to produce ·OH based on the Fenton reaction. And H_2O_2 can also be trapped by Fe^{3+} on the surface of the catalyst, forming Fe^{2+} and completing the cycle of Fe^{2+}/Fe^{3+}. And the generated OH$^-$ could be oxidized by h$^+$ to ·OH. Finally, the produced ·OH can attack the benzene molecules to form hydroxyl cyclohexadienyl radical. After losing a proton, phenol was generated.[58–63]
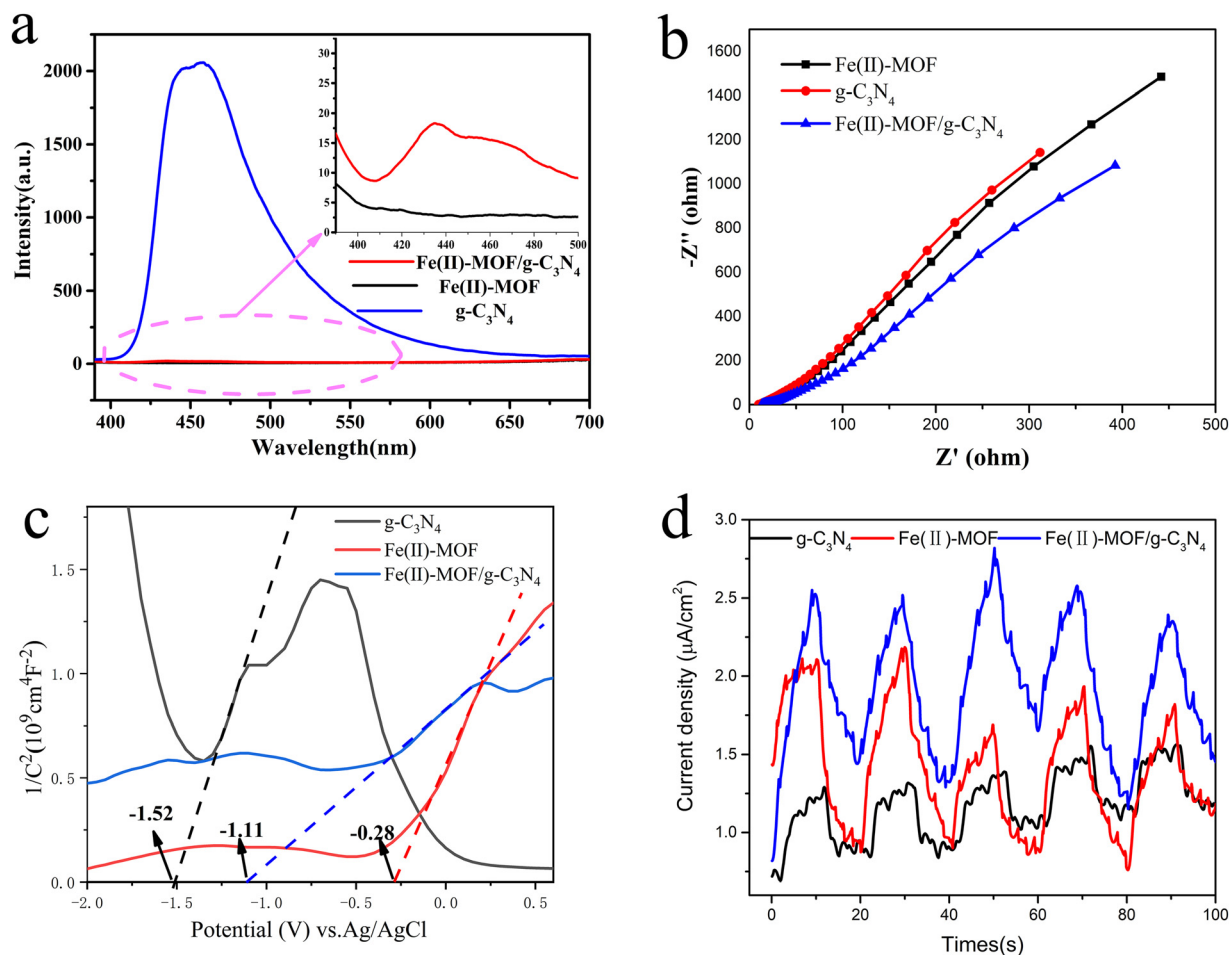
$$\text{Fe(II)-system} \xrightarrow{h\nu} \text{h}^+ + \text{e}^-$$

$$\text{Fe(II)-system} + H_2O_2 \rightarrow \text{Fe(III)-system} + \cdot\text{OH} + \text{OH}^-$$

$$\text{Fe(III)-system} + H_2O_2 \rightarrow \text{Fe(II)-system} + \cdot O_2H + H^+$$

$$\text{OH}^- + \text{h}^+ \rightarrow \cdot\text{OH}$$

$$C_6H_6 + \cdot\text{OH} + \text{h}^+ \rightarrow C_6H_6O + H^+$$

Fig. 6 Photoluminescence profiles (a) of Fe(II)-MOF, layered g-C$_3$N$_4$, and Fe(II)-MOF/g-C$_3$N$_4$, electrochemical impedance profiles (b) and Mot−Schottky diagram (c) of Fe(II)-MOF and Fe(II)-MOF/g-C$_3$N$_4$. Reaction conditions: catalyst (20 mg), benzene (1.6 mL, 18.05 mmol), H$_2$O$_2$ (30 wt%) (0.6 mL), acetonitrile: 11 mL, trifluoroacetic acid: 0.1 g, t = 4 h and T = 333 K.
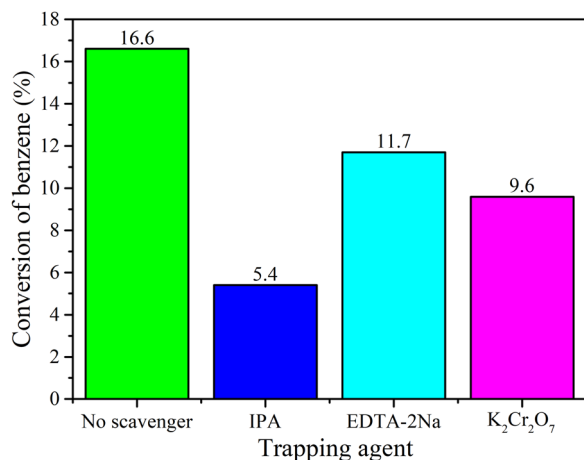

Fig. 7 Free-radical trapping experiments.

Fig. 8 Schematic diagram of the photocatalytic mechanism.

Conclusions

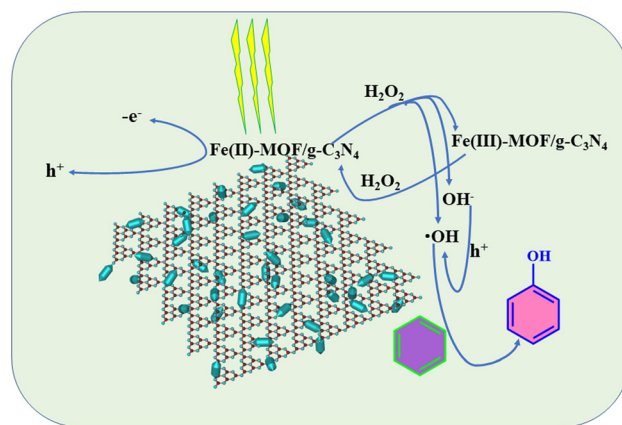In summary, Fe(II)-MOF/g-C$_3$N$_4$ was successfully prepared by the recombination of the Fe(II)-MOF and g-C$_3$N$_4$ via an *in situ* composite technique. The catalyst could achieve direct hydroxylation of benzene under optimal conditions, with a yield and selectivity of 16.4% and 98.9%, respectively. The catalyst could still maintain high photocatalytic activity after 5 cycles. Therefore, due to the efficient catalytic activity and regeneration

performance, the heterogeneous photocatalyst Fe(II)-MOF/g-C_3N_4 showed great potential in the field of benzene hydroxylation to phenol and provided new enlightenment for this field.

Conflicts of interest

There are no conflicts to declare.

Acknowledgements

Notes and references

1 Y. Elkasabi, K. Jones and C. A. Mullen, et al., Spinning band distillation of biomass pyrolysis oil phenolics to produce pure phenol, Sep. Purif. Technol., 2023, 123603.

2 Z. H. Yu, Y. L. Gan and J. Xu, et al., Direct catalytic hydroxylation of benzene to phenol catalyzed by $FeCl_3$ supported on exfoliated graphitic carbon nitride, Catal. Lett., 2020, 150, 301–311.

3 W. Han, W. Xiang and J. Shi, et al., Recent Advances in the Heterogeneous Photocatalytic Hydroxylation of Benzene to Phenol, Molecules, 2022, 27(17), 5457.

4 X. Sun, S. Jiang and H. Huang, et al., Solar energy catalysis, Angew. Chem., Int. Ed., 2022, 134(29), e202204880.

5 S. Li, F. Wu and R. Lin, et al., Enabling photocatalytic hydrogen production over Fe-based MOFs by refining band structure with dye sensitization, Chem. Eng. J., 2022, 429, 132217.

6 D. Wang and Z. Li, Iron-based metal–organic frameworks (MOFs) for visible-light-induced photocatalysis, Res. Chem. Intermed., 2017, 43, 5169–5186.

7 X. Zhang, X. Ma and Y. Ye, et al., Enhanced photocatalytic hydrogen evolution with a Mixed-Valence iron Metal–Organic framework, Chem. Eng. J., 2023, 456, 140939.

8 D. Wang, M. Wang and Z. Li, Fe-based metal–organic frameworks for highly selective photocatalytic benzene hydroxylation to phenol, ACS Catal., 2015, 5(11), 6852–6857.

9 T. N. Tu, H. T. T. Nguyen and H. T. D. Nguyen, et al., A new iron-based metal–organic framework with enhancing catalysis activity for benzene hydroxylation, RSC Adv., 2019, 9(29), 16784–16789.

10 T. Yang, D. Yu and D. Wang, et al., Accelerating Fe(III)/Fe(II) cycle via Fe(II) substitution for enhancing Fenton-like performance of Fe-MOFs, Appl. Catal., B, 2021, 286, 119859.

11 D. Masih, Y. Ma and S. Rohani, Graphitic C_3N_4 based noble-metal-free photocatalyst systems: a review, Appl. Catal., B, 2017, 206, 556–588.

12 S. Verma, R. B. Nasir Baig and M. N. Nadagouda, et al., Hydroxylation of Benzene via C–H activation using bimetallic CuAg@g-C_3N_4, ACS Sustainable Chem. Eng., 2017, 5(5), 3637–3640.

13 S. Su, Z. Xing and S. Zhang, et al., Ultrathin mesoporous g-C_3N_4/NH_2-MIL-101(Fe) octahedron heterojunctions as efficient photo-Fenton-like system for enhanced photo-thermal effect and promoted visible-light-driven photocatalytic performance, Appl. Surf. Sci., 2021, 537, 147890.

14 J. Fu, J. Yu and C. Jiang, et al., g-C_3N_4-Based heterostructured photocatalysts. Advanced Energy, Materials, 2018, 8(3), 1701503.

15 Y. Qi, J. Xu and Y. Fu, et al., Metal–Organic Framework Templated Synthesis ofg-C_3N_4/Fe_2O_3@FeP Composites for Enhanced Hydrogen Production, ChemCatChem, 2019, 11(15), 3465–3473.

16 X. Xu, Y. Chen and Y. Zhang, et al., Highly stable and biocompatible hyaluronic acid-rehabilitated nanoscale MOF-Fe^{2+} induced ferroptosis in breast cancer cells, J. Mater. Chem. B, 2020, 8(39), 9129–9138.

17 D. Huang, Z. Li and G. Zeng, et al., Megamerger in photocatalytic field: 2D g-C_3N_4 nanosheets serve as support of 0D nanomaterials for improving photocatalytic performance, Appl. Catal., B, 2019, 240, 153–173.

18 F. Wei, D. Chen and Z. Liang, et al., Preparation of Fe-MOFs by microwave-assisted ball milling for reducing Cr(VI) in wastewater, Dalton Trans., 2017, 46(47), 16525–16531.

19 S. B. Vuggili, U. K. Gaur and M. Sharma, 2D/2D facial interaction of nitrogen-doped g-C_3N_4/In_2S_3 nanosheets for high performance by visible-light-induced photocatalysis, J. Alloys Compd., 2022, 902, 163757.

20 X. Zhang, X. Song and J. Wang, et al., CO_2 gasification of Yangchangwan coal catalyzed by iron-based waste catalyst from indirect coal-liquefaction plant, Fuel, 2021, 285, 119228.

21 A. Rm, B. Mm and A. Apgp, Synthesis of g-C_3N_4/ZnO heterostructure photocatalyst for enhanced visible degradation of organic dye – ScienceDirect, Optik, 2021, 229, 165548.

22 Y. O. Ibrahim and M. A. Gondal, Visible-light-driven photocatalytic performance of a Z-scheme based TiO_2/WO_3/g-C_3N_4ternary heterojunctions, Mol. Catal., 2021, 505, 111494.

23 M. Chen, W. Chang and Y. Shi, et al., Design of highly efficient g-C_3N_4-based metal monoatom catalysts by two extra-NM_1 atoms: density functional theory simulations, Phys. Chem. Chem. Phys., 2021, 23(19), 11472–11478.

24 P. Xiao, Y. Wang and R. Osuga, et al., One-pot synthesis of highly active Fe-containing MWW zeolite catalyst: Elucidation of Fe species and its impact on catalytic performance, Adv. Powder Technol., 2021, 32(4), 1070–1080.

25 T. Zhao, C. Cheng and D. Wang, et al., Preparation of a bimetallic NiFe-MOF on nickel foam as a highly efficient electrocatalyst for oxygen evolution reaction, ChemistrySelect, 2021, 6(6), 1320–1327.

26 J. R. Zhang, Y. Ma and S. Y. Wang, et al., Accurate K-edge X-ray photoelectron and absorption spectra of g-C_3N_4 nanosheets by first-principles simulations and reinterpretations, Phys. Chem. Chem. Phys., 2019, 21(41), 22819–22830.

27 M. Yu, H. Liang and R. Zhan, *et al.*, Sm-doped g-C_3N_4/Ti_3C_2 MXene heterojunction for visible-light photocatalytic degradation of ciprofloxacin, *Chin. Chem. Lett.*, 2021, **32**(7), 2155–2158.

28 W. B. Mi, E. Y. Jiang and H. L. Bai, Fe^{3+}/Fe^{2+} ratio controlled magnetic and electrical transport properties of polycrystalline $Fe_{3(1-\delta)}O_4$ films, *J. Phys. D: Appl. Phys.*, 2009, **42**(10), 105007.

29 T. Yamashita and P. Hayes, Analysis of XPS spectra of Fe^{2+} and Fe^{3+} ions in oxide materials, *Appl. Surf. Sci.*, 2008, **254**(8), 2441–2449.

30 S. J. Roosendaal, B. Van Asselen and J. W. Elsenaar, *et al.*, The oxidation state of Fe (100) after initial oxidation in O_2, *Surf. Sci.*, 1999, **442**(3), 329–337.

31 P. C. J. Graat and M. A. J. Somers, Simultaneous determination of composition and thickness of thin iron-oxide films from XPS Fe 2p spectra, *Appl. Surf. Sci.*, 1996, **100**, 36–40.

32 X. Wei, N. Zhu and X. Huang, *et al.*, Efficient degradation of sodium diclofenac *via* heterogeneous Fenton reaction boosted by Pd/Fe@Fe_3O_4 nanoparticles derived from bio-recovered palladium, *J. Environ. Manage.*, 2020, **260**, 110072.

33 P. P. Xu, L. Zhang and X. Jia, *et al.*, A novel heterogeneous catalyst NH_2-MIL-88/$PMo_{10}V_2$ for the photocatalytic activity enhancement of benzene hydroxylation, *Catal. Sci. Technol.*, 2021, **11**(19), 6507–6515.

34 Y. Shen, J. Yang and C. Ma, *et al.*, Removal of VOCs from wood by introducing activators to form hydroxyl radicals *in situ* generation platform, *J. Environ. Chem. Eng.*, 2022, **10**(6), 108551.

35 Q. Zhang, M. He and X. Zhang, *et al.*, Tumor microenvironment Activated Chemodynamic–Photodynamic Therapy by multistage self-Assembly engineered protein nanomedicine, *Adv. Funct. Mater.*, 2022, **32**(17), 2112251.

36 B. T. Zhang, Z. Yan and Y. Liu, *et al.*, Nanoconfinement in advanced oxidation processes, *Crit. Rev. Environ. Sci. Technol.*, 2023, **53**(12), 1197–1228.

37 Y. Zhang, H. Wang and T. Zhang, *et al.*, Improving permselectivity of the polyamide reverse osmosis membrane by a controlled-release sulfate radical modification, *Sep. Purif. Technol.*, 2023, 124067.

38 D. Xu, Q. Duan and Y. Hui, *et al.*, Photodynamic therapy based on porphyrin-based metal–organic frameworks, *J. Mater. Chem. B*, 2023, DOI: 10.1039/D2TB02789E.

39 Z. He, Y. Liu and Y. Xiao, Optimization of Fenton pretreatment for 2-chlorophenol solution, *J. Cent. South Univ.*, 2013, **20**(10), 2791–2795.

40 G. Grigoropoulou, J. H. Clark and J. A. Elings, Recent developments on the epoxidation of alkenes using hydrogen peroxide as an oxidant, *Green Chem.*, 2003, **5**(1), 1–7.

41 M. V. Kirillova, Y. N. Kozlov and L. S. Shul'pina, *et al.*, Remarkably fast oxidation of alkanes by hydrogen peroxide catalyzed by a tetracopper(II) triethanolaminate complex: Promoting effects of acid co-catalysts and water, kinetic and mechanistic features, *J. Catal.*, 2009, **268**(1), 26–38.

42 D. Bianchi, R. Bortolo and R. Tassinari, *et al.*, A novel iron-based catalyst for the biphasic oxidation of benzene to phenol with hydrogen peroxide, *Angew. Chem., Int. Ed.*, 2000, **112**(23), 4491–4493.

43 L. Carneiro and A. R. Silva, Selective direct hydroxylation of benzene to phenol with hydrogen peroxide by iron and vanadyl based homogeneous and heterogeneous catalysts, *Catal. Sci. Technol.*, 2016, **6**(22), 8166–8176.

44 K. Jaiswal, M. Mahanta and M. De, Nanomaterials in photocatalysed organic transformations: development, prospects and challenges, *Chem. Commun.*, 2023, **59**, 5987–6003.

45 A. Conde, M. M. Diaz-Requejo and P. J. Pérez, Direct, copper-catalyzed oxidation of aromatic C–H bonds with hydrogen peroxide under acid-free conditions, *Chem. Commun.*, 2011, **47**(28), 8154–8156.

46 S. Farahmand, M. Ghiaci and S. Asghari, Oxo-vanadium(IV) phthalocyanine implanted onto the modified SBA-15 as a catalyst for direct hydroxylation of benzene to phenol in acetonitrile-water medium: A kinetic study, *Chem. Eng. Sci.*, 2021, **232**, 116331.

47 H. Liang, Z. Fang and D. Wei, *et al.*, Improved durability and activity of $FeVO_4$ toward photocatalytic benzene hydroxylation by atomic layer deposited Al_2O_3, *ChemistrySelect*, 2022, **7**(29), e202201044.

48 B. Yang, S. Zhang and Y. Gao, *et al.*, Unique functionalities of carbon shells coating on $ZnFe_2O_4$ for enhanced photocatalytic hydroxylation of benzene to phenol, *Appl. Catal., B*, 2022, **304**, 120999.

49 S. Asghari, S. Farahmand and J. S. Razavizadeh, *et al.*, One-step photocatalytic benzene hydroxylation over iron(II) phthalocyanine: A new application for an old catalyst, *J. Photochem. Photobiol., A*, 2020, **392**, 112412.

50 Y. Fang, L. Zhang and Q. Zhao, *et al.*, Highly selective visible-light photocatalytic benzene hydroxylation to phenol using a new heterogeneous photocatalyst UiO-66-NH2-SA-V, *Catal. Lett.*, 2019, **149**, 2408–2414.

51 X. Chen, J. Zhang and X. Fu, *et al.*, Fe-g-C_3N_4-catalyzed oxidation of benzene to phenol using hydrogen peroxide and visible light, *J. Am. Chem. Soc.*, 2009, **131**(33), 11658–11659.

52 T. Van Tran, V. H. Nguyen and L. X. Nong, *et al.*, Hexagonal Fe-based MIL-88B nanocrystals with NH_2 functional groups accelerating oxytetracycline capture *via* hydrogen bonding, *Surf. Interfaces*, 2020, **20**, 100605.

53 L. Sang, Y. Cheng and R. Yang, *et al.*, Polyphosphazene-wrapped Fe–MOF for improving flame retardancy and smoke suppression of epoxy resins, *J. Therm. Anal. Calorim.*, 2021, **144**, 51–59.

54 X. Dang, R. Yang and Z. Wang, *et al.*, Efficient visible-light activation of molecular oxygen to produce hydrogen peroxide using P doped g-C_3N_4 hollow spheres, *J. Mater. Chem. A*, 2020, **8**(43), 22720–22727.

55 S. Zhao and X. Zhao, Insights into the role of singlet oxygen in the photocatalytic hydrogen peroxide production over polyoxometalates-derived metal oxides incorporated into graphitic carbon nitride framework, *Appl. Catal., B*, 2019, **250**, 408–418.

56 L. Li, J. Wu and B. Liu, *et al.*, NiS sheets modified CdS/reduced graphene oxide composite for efficient visible light photocatalytic hydrogen evolution, *Catal. Today*, 2018, **315**, 110–116.

57 B. Han, X. Li and Z. Zhang, *et al.*, A novel strategy to research the mechanism of rutile TiO$_2$ with excellent photocatalytic performance, *Nanotechnology*, 2021, **33**(3), 035704.

58 F. Zhu, S. Zhou and M. Sun, *et al.*, Heterogeneous activation of persulfate by Mg doped Ni (OH)$_2$ for efficient degradation of phenol, *Chemosphere*, 2021, 131647.

59 S. J. Feng, B. Yue and Y. Wang, *et al.*, Hydroxylation of benzene over V-HMS catalysts with the addition of Fe as the second metal component, *Acta Phys.-Chim. Sin.*, 2011, **27**(12), 2881–2886.

60 Z. Yang, Z. Wang and J. Wang, *et al.*, Facet-Dependent Activation of Oxalic Acid over Magnetic Recyclable Fe$_3$S$_4$ for Efficient Pollutant Removal under Visible Light Irradiation: Enhanced Catalytic Activity, DFT Calculations, and Mechanism Insight, *Environ. Sci. Technol.*, 2022, **56**(24), 18008–18017.

61 J. Li, C. Xiao and K. Wang, *et al.*, Enhanced generation of reactive oxygen species under visible light irradiation by adjusting the exposed facet of FeWO$_4$ nanosheets to activate oxalic acid for organic pollutant removal and Cr(vi) reduction, *Environ. Sci. Technol.*, 2019, **53**(18), 11023–11030.

62 Z. Wang, L. Jiang and K. Wang, *et al.*, Novel AgI/BiSbO$_4$ heterojunction for efficient photocatalytic degradation of organic pollutants under visible light: interfacial electron transfer pathway, DFT calculation and degradation mechanism study, *J. Hazard. Mater.*, 2021, **410**, 124948.

63 T. Guo, L. Jiang and K. Wang, *et al.*, Efficient persulfate activation by hematite nanocrystals for degradation of organic pollutants under visible light irradiation: Facet-dependent catalytic performance and degradation mechanism, *Appl. Catal., B*, 2021, **286**, 119883.